Scintillation index of high frequency acoustic signals forward scattered by the ocean surface

Benjamin Cotté,[a] R. Lee Culver, and David L. Bradley
Graduate Program in Acoustics and Applied Research Laboratory, The Pennsylvania State University, P.O. Box 30, State College, Pennsylvania 16804

(Received 13 April 2006; revised 27 September 2006; accepted 3 October 2006)

Ocean measurements of the scintillation index (SI) of surface forward-scattered signals made in August 2002 are presented and compared with a model developed by Yang and McDaniel [Waves in Random Media **1**, 419–439 (1991)]. The acoustic measurements employed continuous wave (CW) pulses and linear frequency modulated (LFM) sweeps with center frequencies of 20 and 40 kHz. Simultaneously, measurements of wind speed, directional surface wave height spectrum, and ocean sound speed profile were made. The sea state was between 0 and 1 during the four days of the experiment, in part because the location is very much in the lee of San Clemente Island. The measured values of SI are found to agree with Yang and McDaniel model predictions, except for measurements with the largest signal bandwidth and/or the narrowest beamwidths, which violate model assumptions of continuous signals and omnidirectional projectors and hydrophones. In addition, the data show that SI decreases with increasing signal bandwidth (or decreasing temporal extent). An extension to the Yang and McDaniel model is developed that accounts for a reduction in signal temporal extent or ocean surface ensonification. The extended model is in qualitative agreement with the measurements, in that SI is predicted to decrease with increasing signal bandwidth. [DOI: 10.1121/1.2382457]

PACS number(s): 43.30.Re, 43.30.Hw [SLB] Pages: 120–131

I. INTRODUCTION

The intensity of a received signal can display temporal variations due to phenomenon such as relative motion between a source and a receiver, fluctuations in the index of refraction along the propagation path, or motion of the ocean medium. The intensity variance divided by the square of the mean intensity, referred to as the *scintillation index* (SI), is widely used in underwater acoustics to quantify signal level variation.

$$\mathrm{SI} = \frac{\langle I^2 \rangle}{\langle I \rangle^2}. \tag{1}$$

This paper presents measurements and theory for the SI of acoustic signals that have been forward scattered by the ocean surface. This work represents the first measurement-model comparison for the SI ocean surface forward-scattered signals.

From a theoretical point of view, there are several models for the SI of surface forward-scattered signals (Macaskill and Kachoyan, 1988; Frankenthal, 1990; Yang and McDaniel, 1991). The Yang and McDaniel (henceforth referred to as YMcD) model is the focus of this paper. It involves a scattering strength or roughness parameter that is proportional to the ratio of root mean square (rms) ocean surface wave height to acoustic wavelength. When the strength/roughness parameter is small, scattering is weak and the SI is close to 0; this is called *unsaturated* scattering by Flatté (1983) in the context of scattering by ocean volume inhomogeneities. When the strength/roughness parameter is large, scattering is strong and the SI approaches 1; this is called *saturated* scattering. The SI can follow two behaviors in the transition region, as shown in Fig. 1 (Colosi and Baggeroer, 2004), which was developed from ocean volume scattering considerations but is (shown to be, in Sec. II) applicable to scattering by the ocean surface. In the diffractive path to saturation, the SI increases monotonically from 0 to 1 in transitioning from unsaturated to saturated scattering. In the geometric path to saturation, the SI reaches a maximum and decreases to 1. In this case, SI values greater than 1 can occur due to constructive and destructive interference between a few, discrete acoustic paths (Flatté, 1983; Colosi and Baggeroer, 2004); this phenomenon is referred to as *partially saturated* scattering. The behavior in the partially saturated region is controlled by scatterer size or (for the purposes of this work) a diffraction parameter related to the size of the first Fresnel zone relative to the correlation length of surface height fluctuations. Both the strength/roughness and size/diffraction parameters will be discussed in detail below.

From an experimental point of view, there are few published measurements of SI for ocean surface forward-scattered signals. Several papers published in the 1960s and 1970s dealt with second order moments of the scattered pressure (Scrimger, 1961; Melton and Horton, 1970; Nichols and Senko, 1974). More recently, Stroud, Marston, and Williams (1997) published theoretical predictions and experimental data for fourth order (and higher) moments of the scattered pressure. The measurements were conducted in a tank using a rigid one-dimensional surface with a Gaussian roughness spectrum. Their experiment showed that SI falls off as pulse

[a]Present address: Ecole Centrale de Lyon, Laboratoire de Mécanique des Fluides et d'Acoustique, UMR CNRS 5509, BP 163, 69131 Ecully Cedex, France. Electronic address: benjamin.cotte@ec-lyon.fr

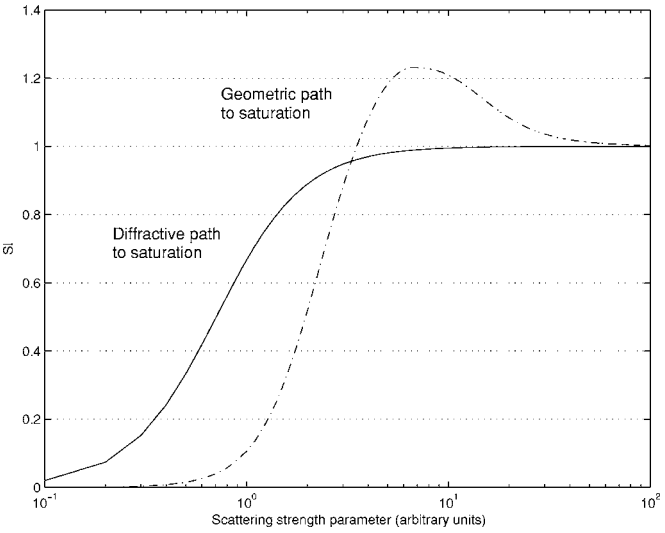

FIG. 1. Sketch of SI vs strength parameter illustrating the two possible paths to saturation. After Colosi and Baggeroer (2004, Fig. 1).

length is reduced in the saturated region, which is consistent with the measurements presented in this report.

This paper presents measurements of the SI of surface forward-scattered signals made in August 2002 near the eastern shore of San Clemente Island, California, and compares them with theory developed by Yang and McDaniel (1991) (YMcD). The acoustic measurements employed 1.0 and 0 .14 ms continuous wave (CW) pulses and 8 ms linear frequency modulated (LFM) sweeps with center frequencies of 20 and 40 kHz; LFM signal bandwidths range from 1 to 22 kHz. Source-receiver separation was approximately 700 m. In most cases, source and receiver depths were such that the direct and surface forward-reflected arrivals were separated in time. Environmental measurements of the wind speed, the directional surface wave height spectrum, and the ocean sound speed profile accompanied the acoustic measurements. The sea state was between 0 and 1 during the experiment, in part because the location is very much in the lee of San Clemente Island.

As will be discussed in Sec. II, the YMcD model is based upon the Kirchhoff approximation for scattering from the rough surface. Thus the issue of the validity of the Kirchhoff approximation for the experimental conditions associated with the measurements presented in this paper has to be considered. Thorsos (1988; 1990) has investigated the conditions under which the Kirchhoff approximation is valid and found it accurate near the specular direction, even for quite small incident angles (as low as 10 deg). Both single spatial scale Gaussian and multiscale Pierson-Moskowitz surface wave height distributions were considered. Away from specular, but still far from very shallow grazing angles where shadowing or multiple scatter can occur, the validity of the Kirchhoff approximation was found to depend upon the ratio of the surface correlation length l to the acoustic wavelength λ. This is the range of angles which dominate the scintillation of forward-scattered signals, and here the Kirchhoff approximation is found to be valid as long as $\frac{l}{\lambda} > 1$. For the data presented here, the grazing angles are 10 to 20 deg; values of l range from 0.6 to 4.9 m and λ is 0.0325 or

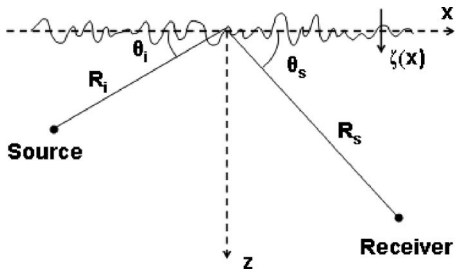

FIG. 2. Geometry for the YMcD model for scintillation index (SI).

0.075 m (see Sec. IV), so that $\frac{l}{\lambda}$ is clearly much greater than 1. The validity of the Kirchhoff approximation is therefore valid and it is appropriate to compare the YMcD model with the measurements.

The experimental conditions did not satisfy two important assumptions of the YMcD model, namely, that the signal was continuous and the projector and hydrophones were omnidirectional. The measurements were made with pulses with finite bandwidth (larger than 1 kHz), and half of the acoustic projectors and all of the receive hydrophones were directional. Not withstanding these shortcomings, many SI measurements agree well with the YMcD model. The SI measurements that did not agree with the model were made using signals with the largest bandwidth and/or projectors/hydrophones that ensonified a significantly reduced area of the ocean surface, thus violating model assumptions to the greatest degree. Increasing signal bandwidth results in increased temporal resolution at the output of the matched filter, and equivalently in reduced signal temporal extent. The YMcD development has been modified to handle pulses with finite bandwidth and directional beams by limiting the ensonified area of the ocean surface, hereafter referred to as the XYMcD model. The XYMcD model predicts a reduction in SI when the signal temporal extent is shortened, which is in agreement with the measurements.

The Yang and McDaniel (YMcD) model and its extension for limited ensonification of the ocean surface (XYMcD) are described in Secs. II and III, respectively. In Sec. IV acoustic and environmental measurements are presented, and the method of estimating the surface wave height spectrum and the correlation function of surface wave height fluctuations is detailed. SI measurements are compared to YMcD and XYMcD model predictions in Secs. V and VI, and a summary is given in Sec. VII.

II. THE YANG AND MCDANIEL (YMcD) MODEL FOR SCINTILLATION INDEX (SI)

The Yang and McDaniel (YMcD) model (Yang and McDaniel, 1991) utilizes the two-dimensional geometry shown in Fig. 2 and assumes an omnidirectional source and receiver, a CW signal, and validity of the Kirchhoff approximation. Derivation of the scattered pressure for the Kirchhoff approximation is taken from Clay and Medwin (1977). Using the geometry and notation of Fig. 2 and the assumptions discussed above, the scattered pressure p_s can be written

$$p_s = \int_{-\infty}^{\infty} \exp\left[-i\left(\frac{x^2}{x_f^2} + 2\gamma\zeta(x) \right) \right] dx, \tag{2}$$

where

$$x_f^2 \equiv \frac{2}{k}\left(\frac{\sin^2\theta_i}{R_i} + \frac{\sin^2\theta_s}{R_s} \right)^{-1}, \tag{3}$$

$$\gamma \equiv -\frac{k}{2}(\sin\theta_i + \sin\theta_s). \tag{4}$$

In writing Eq. (2), the terms describing time and range dependence have been omitted because they are not important to this derivation. Note that $\zeta(x)$ denotes surface elevation. The parameter x_f can be interpreted as $\frac{1}{\sqrt{\pi}}$ times the radius of the first Fresnel zone (Clay and Medwin, 1977, p. 50), projected onto the x axis. The $\exp\left(-i\frac{x^2}{x_f^2}\right)$ term thus provides sinusoidal dependence upon x as x moves through the Fresnel zones. Also, k is the wave number and γ is the mean vertical component of the wave number of the incident and scattered waves, so that the term $2\gamma\zeta(x)$ parametrizes the effect of the rough surface to alter the phase of the received signal (Clay and Medwin, 1977, p. 340). Equation (2) is the starting point for calculating the mean intensity $\langle I\rangle = \langle |p_s|^2\rangle$ and the mean squared intensity $\langle I^2\rangle = \langle |p_s|^4\rangle$. After some manipulations, Yang and McDaniel obtain the following expression for SI:

$$\begin{aligned} \mathrm{SI} &= \frac{\langle I^2\rangle}{\langle I\rangle^2} - 1 \\ &= \frac{4}{\pi}\,\mathrm{Re}\left[\int_0^{\infty} \left(\int_0^{P} \exp(-iPS)\exp[-\Phi^2 H(P,S)]\,dS \right) dP \right] \\ &\quad - 1, \end{aligned} \tag{5}$$

where Re means "real part of," and P and S are functions of position on the surface defined for convenience. Equation (5) is the same as Eq. (32) of YMcD. It is similar to Eq. (9) of Yang, Fennemore, and McDaniel (1992), in which the YMcD theory is applied to a two-dimensional (2D) ocean surface; note that for consistency the factor in front of the integral should be $\frac{4}{\pi}$ in the latter paper. The factor H depends on the correlation function of a nondimensional parameter $C(X) = C_\zeta\left(\frac{Xx_f}{\sqrt{2}}\right) = C_\zeta(Xl\sqrt{\Lambda})$

$$H(P,S) = 2 - 2C(P) - 2C(S) + C(P+S) + C(P-S). \tag{6}$$

Φ and Λ are the strength/roughness and size/diffraction parameters that control SI behavior. They are defined as follows:

$$\Phi^2 \equiv 4h^2\gamma^2, \tag{7}$$

$$\Lambda \equiv \frac{x_f^2}{2l^2}, \tag{8}$$

where $h = \langle \zeta^2\rangle^{1/2}$ is the rms ocean surface wave height and l is the scale size for the ocean surface correlation function.

To understand what Φ and Λ physically mean, consider the case of specular reflection ($\theta_i = \theta_s = \theta$ in Fig. 2). Then Eq. (7) becomes the Rayleigh roughness parameter $\Phi = 4\pi h \sin\theta/\lambda$, where λ is the acoustic wavelength, as defined, for instance, by Melton and Horton (1970) and Dahl (1999).[1] When Φ is large ($\Phi \gg 1$), the surface appears very rough and there are many acoustic paths to the receiver that are, on average, uncorrelated. SI approaches 1, and the scattering is referred to as *saturated*. When Φ is small ($\Phi \ll 1$), the surface appears smooth and approaches only one acoustic path. SI approaches 0, and the scattering is referred to as *unsaturated*. This behavior can be seen on the Λ-Φ diagram shown in Fig. 3 (Flatté, 1983). The axes in Fig. 3 are $\Phi_{\mathrm{Flatte}} = k_0\langle\mu^2\rangle^{1/2}\sqrt{RL_P}$ and $\Lambda_{\mathrm{Flatte}} = R/6L^2k_0$, where $\langle\mu^2\rangle^{1/2}$ is the rms sound speed fluctuation, R is source-receiver separation, L and L_P are the sound speed inhomogeneity correlation lengths in the vertical direction and along the path, respectively, and k_0 is the mean acoustic wave number (Flatté *et al.* 1979). There is strong physical correspondence between Φ_{Flatte} and $\Lambda_{\mathrm{Flatte}}$, which were derived for ocean volume scattering, and Φ and Λ defined in Eqs. (7) and (8) for surface-forward scattering. The rms wave height and correlation length of the ocean surface in the YMcD theory correspond to rms sound speed fluctuation and the correlation length of the sound speed fluctuations, respectively, in Flatté's theory. In both theories, the diffraction parameter Λ is proportional to the square of the Fresnel radius divided by the square of a correlation length. Both definitions of the strength parameter include the product of a wave number and rms fluctuation, but in Flatté's theory an additional range times along-path correlation length term is present. Scattering in the ocean volume occurs along the path, and $\sqrt{RL_P}$ is a Fresnel term with L_P replacing λ.

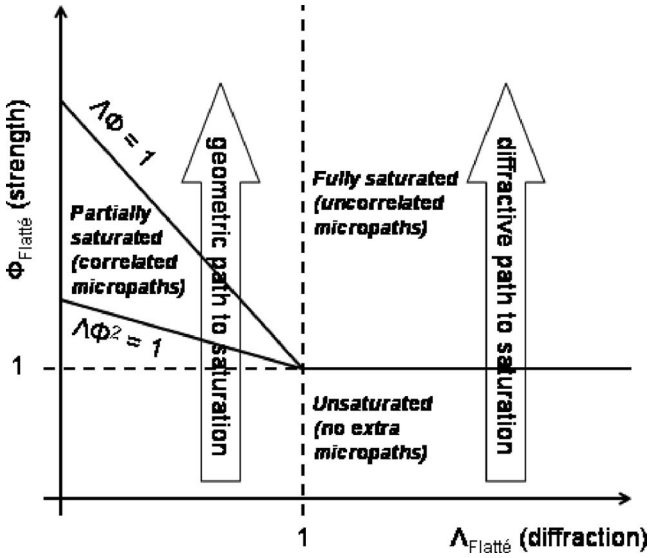

FIG. 3. Λ-Φ diagram representing the different scattering regimes with respect to the size/diffraction parameter $\Lambda_{\mathrm{Flatte}}$ and the strength/roughness parameter Φ_{Flatte}. After Flatté (1983, Fig. 12).

Λ plays an important role in the transition region between the unsaturated and saturated regions in both volume and surface scattering. As stated above, x_f can be interpreted as $\frac{1}{\sqrt{\pi}}$ times the radius of the first Fresnel zone projected onto the x axis. A spherical wave front can be divided into half-wavelength annular zones called Fresnel zones; these zones

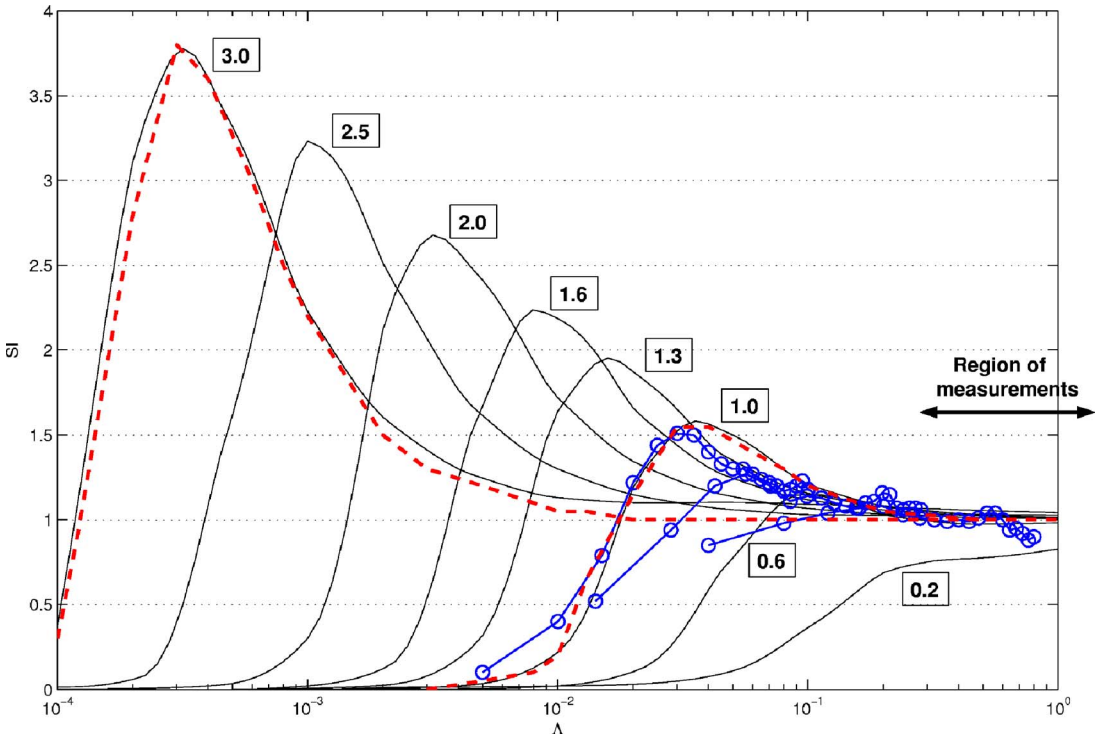

FIG. 4. (Color online) Comparison of three models for SI of ocean forward-scattered signals. A Gaussian surface correlation spectrum is used, and results are plotted and scaled with respect to the Yang and McDaniel Λ and Φ parameters. The Yang and McDaniel predictions are given for $\log_{10}(\Phi)=0.2$, 0.6, 1.0, 1.3, 1.6, 2.0, 2.5, and 3.0 (solid lines), as given in the text boxes. Macaskill and Kachoyan predictions are given for $\log_{10}(\Phi)=0.70$, 0.85, and 1.0 (open circles), and Frankenthal predictions are given for $\log_{10}(\Phi)=1.0$ and 3.0 (dashed lines).

define phase relationships, since points from adjacent zones are out-of-phase from each other. The parameter l is a measure of the area over which the surface elevation is correlated. Thus for surface scattering, Λ compares the size of the first Fresnel zone to the size of the correlated region of the ocean surface, and is therefore called size parameter. Λ provides a similar comparison for volume scattering, although it is called a diffraction parameter by Flatté (1983) since for small values of Λ (roughly $\Lambda<1$), the geometric approximation is valid, while for large values of Λ (roughly $\Lambda>1$), diffraction occurs. The corresponding geometric and diffractive paths to saturation are represented by two block arrows in Fig. 3, which are related to the SI behavior shown in Fig. 1. For surface scattering, in the geometric path to saturation ($x_f<l$), the surface elevation is correlated over several Fresnel zones. This leads to constructive and destructive interference between acoustic arrivals (also referred to as *multipath correlation* by Colosi and Baggeroer (2004)) for a range of Φ values that cause large variations and SI values greater than 1. In the diffractive path to saturation ($x_f>l$), acoustic arrivals from Fresnel zones other than the first zone are uncorrelated and SI transitions directly from unsaturated scattering to fully saturated scattering.

YMcD predictions for dependence of SI on Λ for various values of Φ using a Gaussian surface correlation spectrum are shown in Fig. 4. Note that this representation is different from the one used in Fig. 1. Curves in Fig. 1 are equivalent to vertical paths in the Λ-Φ diagram (see Fig. 3), while curves in Fig. 4 are equivalent to horizontal paths in the Λ-Φ diagram. As will be discussed in Sec. V, the range of Λ values over which measured SI can be compared with the YMcD model is 0.3 to 1.9, and this range is indicated in the figure. Two other models are compared in Fig. 4 using Yang and McDaniel Λ and Φ parameters. The predictions by Macaskill and Kachoyan (1988) are obtained by numerical simulation based upon inversion of the full integral equation describing surface scattering, for which the Kirchhoff approximation corresponds to the first iteration. As shown there and by Thorsos (1988), the Kirchhoff approximation compares well with the full integral equation for scattered angles near the specular, for small to moderate rms surface waveheight, and for a Gaussian surface waveheight spectrum. Reflection coefficients are found for different realizations of a random sea surface, and the SI is calculated by ensemble averaging over the reflection coefficients. No size parameter is explicitly defined. The model by Frankenthal (1990) uses a phase screen model for the surface interaction that can be applied to a refracting as well as a reflecting scattering surface. Numerical results are presented for large scattering strength parameters and for normal incidence. Frankenthal's definition of Λ is the same as Yang and McDaniel's for normal incidence $\left(\theta_i=\theta_s=\frac{\pi}{2}\right)$. It can be seen that his model fits Yang and McDaniel's very well. To calculate Λ using Macaskill and Kachoyan parameters, a rms wave height h (or equivalently a correlation length l) needs to be chosen. h is assumed to be 0.01 m to obtain the best fit with the other two models for $\log_{10}(\Phi)=1.0$. Doing so this model fits the Yang and McDaniel predictions relatively well. Note that all three models predict unsaturated scattering for the smallest values of Φ. They also predict that the peak value of SI above 1,

characteristic of the partially saturated region, increases and shifts to lower Λ as Φ increases. This behavior is consistent with Fig. 3.

III. YMcD MODEL EXTENSION FOR FINITE SIGNAL BANDWIDTH AND LIMITED ENSONIFICATION OF THE OCEAN SURFACE (XYMcD)

The conditions of the SI measurements reported in this paper violate the assumptions of the YMcD model in two respects. First, pulses with finite bandwidth were transmitted rather than continuous signals, and second, directional acoustic projectors and hydrophones were used. A continuous signal has broad temporal extent or equivalently, very small effective bandwidth. The signals used in the 2002 field experiment have small temporal extent or non-zero effective bandwidth, which means that at any given time only a small part of the ocean surface will contribute to the received signal. The size of the area of the ocean surface that contributes to the received signal is limited by the signal characteristics because matched-filtering provides temporal extent equal to the inverse signal bandwidth. For instance, the extent of the ocean surface contributing to the received signal for a 1 ms pure tone pulse and an 8 ms, 1 kHz LFM is approximately $\frac{c}{\beta}=1.5$ m, where $c=1500$ m/s is the speed of sound in the water and β is the effective bandwidth. Similarly, hydrophone directionality resulted in incomplete illumination of the surface for some projector-receiver pairs. In some cases the specular point was not strongly illuminated. Many measured SI values agreed with the YMcD model in spite of these differences, but the SI measurements with the shortest signal temporal extent (or largest bandwidth) and narrowest beams did not agree. Therefore, the YMcD model has been modified to account for finite signal bandwidth and hydrophone beam width by introducing an illumination factor $\mathfrak{I}(x)$ (Clay and Medwin, 1977). The illumination factor $\mathfrak{I}(x)$ is limited to values between 0 and 1 and indicates the combined projector-hydrophone pattern response for the point x on the surface ($x=0$ is the specular point, as may be seen in Fig. 2). $\mathfrak{I}(x)=1$ corresponds to a completely ensonified surface (omnidirectional projectors and hydrophones) and $\mathfrak{I}(x)=0$ corresponds to no ensonification of the surface.

Introducing the illumination factor into the equation for the scattered pressure, Eq. (2) becomes

$$p_s=\int_{-\infty}^{\infty}\mathfrak{I}(x)\exp\left[-i\left(\frac{x^2}{x_f^2}+2\gamma\zeta(x)\right)\right]dx. \tag{9}$$

Equation (9) has been evaluated by Clay and Medwin (1977) for the case of a Gaussian beam. The mean intensity is given by

$$\langle I\rangle = x_f^2\int_0^{\infty}\left[\int_{-\infty}^{\infty} IL'(\omega,\xi)\cos(\omega\xi)d\omega\right] \times\exp[-\Phi^2(1-C(\xi))]d\xi, \tag{10}$$

where

$$IL'(\omega,\xi)=\mathfrak{I}\left(\frac{x_f}{\sqrt{2}}\omega+\frac{x_f}{2\sqrt{2}}\xi\right)\mathfrak{I}\left(\frac{x_f}{\sqrt{2}}\omega-\frac{x_f}{2\sqrt{2}}\xi\right). \tag{11}$$

A quadruple integral must be evaluated in order to calculate the mean squared intensity

$$\langle I^2\rangle=\frac{x_f^4}{4}\int_{-\infty}^{\infty}\int_{-\infty}^{\infty}\left[\int_{-\infty}^{\infty}\int_{-\infty}^{\infty} IL(t,P,S,q) \times\exp(-itq)\exp[\Phi^2H_1(P,S,q)]dtdq\right] \times\exp(-iPS)\exp[-\Phi^2H_2(P,S)]dSdP, \tag{12}$$

where t and q are temporary variables of integration with no physical significance

$$H_1(P,S,q)=C\left(P+\frac{q}{2}\right)+C\left(P-\frac{q}{2}\right)+C\left(S+\frac{q}{2}\right)+C\left(S-\frac{q}{2}\right),$$

$$H_2(P,S)=2+2C(P+S)+C(S-P), \tag{13}$$

and

$$\begin{aligned}IL(t,P,S,q)=&\,\mathfrak{I}\left(\frac{x_f}{\sqrt{2}}t+\frac{x_f}{2\sqrt{2}}P+\frac{x_f}{2\sqrt{2}}S+\frac{x_f}{4\sqrt{2}}q\right)\\&+\mathfrak{I}\left(\frac{x_f}{\sqrt{2}}t-\frac{x_f}{2\sqrt{2}}P+\frac{x_f}{2\sqrt{2}}S-\frac{x_f}{4\sqrt{2}}q\right)\\&+\mathfrak{I}\left(\frac{x_f}{\sqrt{2}}t-\frac{x_f}{2\sqrt{2}}P-\frac{x_f}{2\sqrt{2}}S+\frac{x_f}{4\sqrt{2}}q\right)\\&+\mathfrak{I}\left(\frac{x_f}{\sqrt{2}}t+\frac{x_f}{2\sqrt{2}}P-\frac{x_f}{2\sqrt{2}}S-\frac{x_f}{4\sqrt{2}}q\right).\end{aligned} \tag{14}$$

The effect of the illumination factor on SI has been evaluated using the XYMcD model and an illumination factor defined by

$$\mathfrak{I}_{x_0}\equiv\begin{cases}\dfrac{1+\cos\left(\dfrac{\pi x}{2x_0}\right)}{2} & \text{for } x\le 2x_0,\\ 0 & \text{elsewhere,}\end{cases} \tag{15}$$

where x_0 parametrizes the width of the ensonified area. In Fig. 5, SI is plotted versus x_0 for different values of $\log_{10}(\Phi)$. It can be seen that SI decreases as the size of the ensonified area decreases. As mentioned earlier, the range of Λ values used for comparison with measured SI is 0.3 to 1.9. Results are shown for Λ equal to 0.5 only in Fig. 5 since extended model predictions depend very little on the size parameter Λ for Λ between 0.3 and 1.9.

IV. OCEAN MEASUREMENTS

Acoustic and environmental measurements were made over a four-day period during August 2002 about 2.5 km east of San Clemente Island, California (32° 38.2′ N, 117° 57.4′ W). Water depth was approximately 500 m. The acoustic

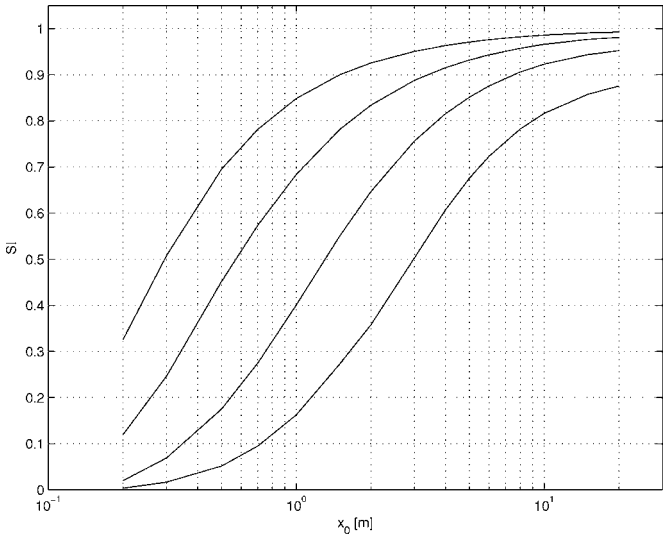

FIG. 5. XYMcD model predictions calculated using the illumination factor $\mathfrak{I}_{x_0}$ and the swell enhanced Plant spectrum described in Sec. IV C. $\Lambda=0.5$ for all curves and $\log_{10}(\Phi)=0.4$, 0.6, 0.8, and 1.0 from the lowest to the highest curve.

measurement system and the signals used to measure SI are described in Sec. IV A. Environmental measurements are identified in Sec. IV B. The surface waveheight spectrum, the correlation function of surface height fluctuations, the rms waveheight, and the correlation length are estimated in Sec. IV C.

A. Acoustic measurements

The acoustic measurement system consists of four projectors deployed from a moored buoy and a set of six receive hydrophones deployed from the Motor Vessel (M/V) Acoustic Explorer as shown in Fig. 6. Projectors P_1 and P_3 are ITC 6084 hydrophones, with vertical half-beam widths of 13.3° at 20 kHz and 6.4° at 40 kHz. Projectors P_2 and P_4 are ITC 1001 projectors, which are basically omnidirectional. All receive hydrophones are ITC 6080C, which have vertical half-beamwidths of 42.0° at 20 kHz and 20.6° at 40 kHz. Hydrophone H_3 malfunctioned during the experiment and recorded no data. Seven acoustic data sets were recorded during the experiment. Data for projector P_4 were only available for

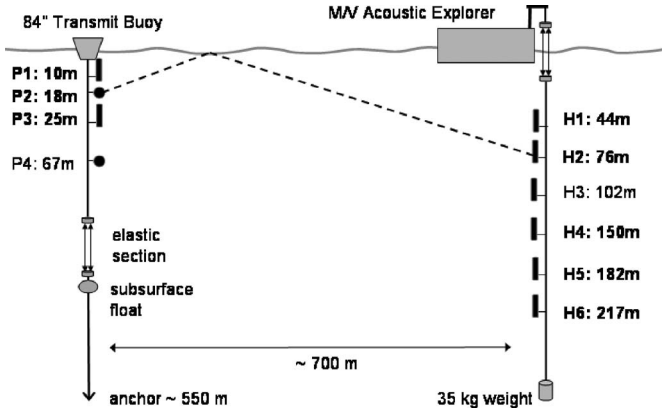

FIG. 6. Acoustic measurement system configuration. The specular ray for *P2-H2* (projector 2 - hydrophone 2) is shown.

TABLE I. Acoustic signal characteristics.

Name	Type	Center frequency (kHz)	Bandwidth (kHz)	Duration (ms)
Short CW 20	CW	20	7	0.14
Long CW 20	CW	20	1	1
Short CW 40	CW	40	7	0.14
Long CW 40	CW	40	1	1
LFM 20-1	LFM	20	1	8
LFM 20-7	LFM	20	7	8
LFM 20-13	LFM	20	13	8
LFM 20-22	LFM	20	22	8
LFM 40-1	LFM	40	1	8
LFM 40-7	LFM	40	7	8
LFM 40-13	LFM	40	13	8
LFM 40-22	LFM	40	22	8

LFM signal duration is 10 ms for projector P3 only.

two of the seven measurement periods and are not used in this paper. Also, direct and surface bounce paths could not be separated for the shallowest projectors and receivers and those data are not used in this paper.

For each data set, the 12 signals identified in Table I were transmitted by each projector. Center frequencies are 20 and 40 kHz. CW signals with duration 0.14 and 1 ms are referred to as "short" and "long" pulses, respectively. LFM signals have bandwidths ranging from 1 to 22 kHz. For each signal and each projector, 300 pings were transmitted using a 0.1 s repetition rate. Received signals from all hydrophones were digitized and recorded simultaneously using a sample rate of 312.5 kHz. Subsequently, received signals were matched filtered and the peak of the filter output located. The SI was calculated over the 300 peak values of the surface scattered path in the match-filtered output.

B. Environmental measurements

Sound speed in the water column, wind speed, and directional surface waveheight spectrum were measured during the four-day period of the experiment. The sound speed profile was estimated approximately once a day using a cast conductivity-temperature-depth (CTD) profiler dropped down to a depth of approximately 300 m. As shown in Fig. 7, a downward refracting profile is found; it is very similar from day to day. Ray tracing is used to determine whether the specular point is strongly illuminated for each projector-receiver pair. The time-averaged directional wave height spectrum was measured every 30 min using a Triaxys Directional wave rider buoy. However, sea surface waveheight during the experiment was too small to be measured accurately by the wave rider buoy[2] and those data are not used in this paper. Wind speed was measured using a Handar ultrasonic anemometer every 10 s, except that there are no wind speed data for one of the four days of the experiment. Measured wind speed ranges from 6 to 12 m/s. Because of the relatively steady conditions, the wind speed is taken to be 8 ± 2 m/s during the experiment. The rms waveheight is very low considering the wind speed measured during the experi-

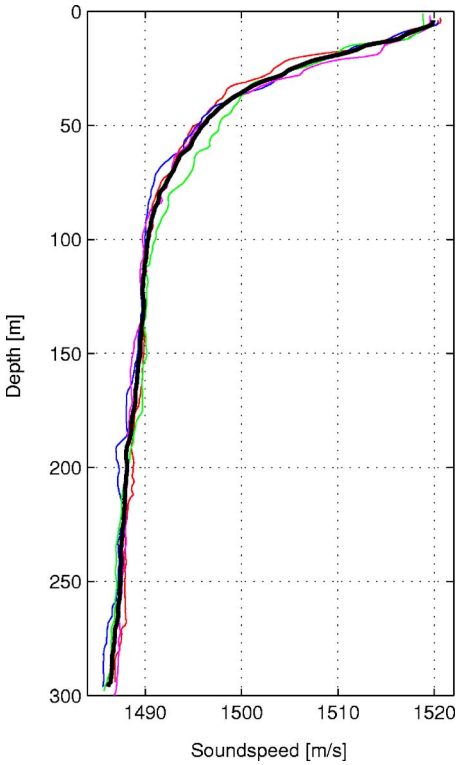

FIG. 7. (Color online) Sound speed profiles measured between 15 and 18 August 2002 at the experiment site (thin lines). The thick line is the averaged sound speed profile over the four days.

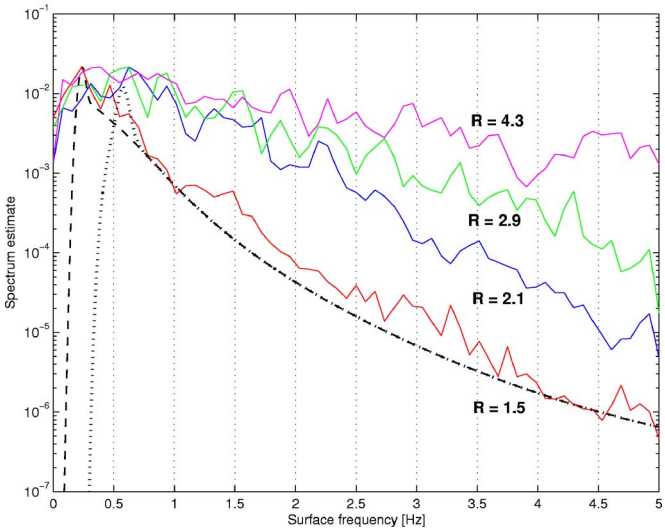

FIG. 8. (Color online) Spectra of peak long pulse acoustic intensity values (solid lines) for different values of the Rayleigh roughness parameter R (as labeled). Each spectrum is an average over three measurement periods. The dotted line corresponds to Plant's model calculated using a wind speed of 8 m/s and a fetch of 2500 m. The dashed line is Plant's model extended to include a swell component at 0.23 Hz. All of the acoustic spectra have been scaled so that their maxima equal the swell enhanced Plant spectrum maximum.

ment; this is because of the close proximity of the experiment to San Clemente Island and the attendant reduced fetch (McDaniel and McCammon, 1987).

C. The surface waveheight spectrum and correlation function

As stated above, surface conditions during the experiment were too benign to be measured by the Triaxys wave rider buoy. However, the correlation function of surface height fluctuations is an important input parameter to the models described in Secs. II and III. Accordingly, a model was employed to estimate the surface waveheight spectrum, the correlation function and the correlation length. Following Dahl (1999), the isotropic correlation function $C_\zeta(\rho)$ can be computed via the Bessel transform relation

$$C_\zeta(\rho) = \frac{\int_0^\infty KJ_0(K\rho)F(K)dK}{\int_0^\infty KF(K)dK}, \tag{16}$$

where K is the magnitude of the ocean surface wave number, $F(K)$ is the directionally averaged surface height wavenumber spectrum, and ρ is the horizontal distance between two points on the surface. Dahl showed that at high acoustic frequencies (approximately 10 kHz and more), directionality of the surface waveheight spectrum does not play an important role since scattering is dominated by capillary waves (Dahl, 1999; Dahl, 2004).

The surface waveheight spectrum has been modelled using Plant's D spectrum (Plant, 2002). The model input parameters are wind speed and fetch. Because the experiment location was about 2500 m east of San Clemente Island, and the wind was out of the west northwest, the fetch is limited to approximately 2500 m. Diffraction around the north-east tip of the island could cause the effective fetch to be higher. On the other hand, because of shadowing by hills on the island, the effective fetch could be lower than 2500 m. For this analysis, the fetch is taken to be 2500 ± 1500 m.

Use of Plant's model with a wind speed of 8 m/s and a fetch of 2500 m produces the waveheight spectrum shown in Fig. 8. The spectra of acoustic intensity fluctuations of selected measurements are also shown in Fig. 8 for comparison. They correspond to Rayleigh roughness parameter $R = 2kh \sin(\theta)$ [see Eq. (7) in the case of specular reflection ($\theta_i = \theta_s = \theta$)] of 1.5 to 4.3, all normalized to the same maximum value. (The variation in R is due to change in grazing angle and acoustic frequency.) A swell enhanced Plant spectrum (explained below) is also plotted in Fig. 8.

It can be observed in Fig. 8 that the acoustic spectrum for the smallest roughness parameter follows Plant's model well above 0.5 Hz. However, as the roughness parameter increases, higher frequency energy increases and a flattening of the acoustic spectrum is observed. As a result, the fit with Plant's model degrades. The spectral broadening is related to the change in the probability density function (pdf) of the peak pressure at the receiver, as described by Clay and Medwin (1977). For small roughness parameter, the scattered pressure follows a Gaussian distribution, and the field is dominated by the coherent contribution corresponding to specular reflection. For the large roughness parameter, the scattered pressure follows a Rayleigh distribution; there are a large number of randomly phased contributions (contribu-

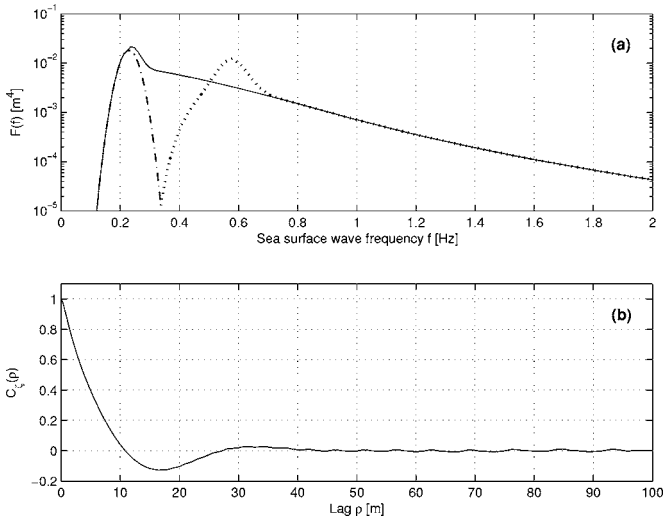

FIG. 9. (a) Directionally averaged wave-number spectra for Plant's model with a wind speed of 8 m/s and a fetch of 2500 m (dotted line), for the Gaussian contribution due to swell centered at 0.23 Hz (dash-dotted line), and for the swell enhanced Plant spectrum (solid line). (b) Correlation function of surface height fluctuations calculated using the swell enhanced Plant spectrum.

tions from many random facets of the ocean surface), and the incoherent component of the field dominates. This broadening of the acoustic spectra for large roughness parameter was observed experimentally by Scrimger (1961) and Brown (1969). The result is that the spectrum of the acoustic pressure (or intensity) fluctuations closely follows the ocean surface fluctuation spectrum for the small roughness parameter, while for larger roughness parameter, the acoustic fluctuation spectra contain high frequency energy that is not present in the surface wave height spectrum.

In general, the peaks of the acoustic spectra in Fig. 8 occur at frequencies below the 0.6 Hz peak of the Plant model spectrum. The acoustic spectrum with the smallest roughness parameter has a peak at 0.23 Hz (with a frequency resolution of 0.04 Hz). This peak could be due to swell from distant storms, which is not predicted by Plant's model, but which could have been diffracted around the northeast tip of San Clemente Island. The peak is modeled as a Gaussian spectrum centered at 0.23 Hz. Taking into account the peak in the acoustic spectra, a new wave-number spectrum is constructed by combining the Gaussian spectrum and Plant's D spectrum extrapolated down to 0.23 Hz. Figure 9(a) illustrates the construction of the swell enhanced Plant spectrum.

Surface waveheight frequency spectra are used to calculate the wave-number spectra, using the dispersion relation

$$(2\pi f)^2 = gK, \tag{17}$$

where f is the surface wave frequency and $g=9.8$ m/s^2 is the gravitational constant. A correlation function calculated using Eq. (16) and the extended waveheight spectrum is plotted in Fig. 9(b). The rms wave height is obtained from the wave spectrum $F(K)$ using

TABLE II. Rms wave height h and correlation length l for Plant's D spectrum, for the swell enhanced Plant spectrum shown in Fig. 9(a), and for two extended spectra illustrating the effect of uncertainties on wind speed, fetch and swell peak frequency.

Type of spectrum	Wind speed (m/s)	Fetch (m)	Peak frequency (Hz)	h (cm)	l (m)
Plant's D spectrum	8	2500	N/A	4.0	0.6
Swell enhanced Plant spectrum	8	2500	0.23	4.4	3.2
"Lowest-energy" spectrum	6	1000	0.27	2.1	2.2
"Highest-energy" spectrum	10	4000	0.19	7.1	4.9

$$h = \sqrt{\langle \zeta^2 \rangle} = \left(\int_0^\infty KF(K)dK \right)^{1/2}. \tag{18}$$

Yang, Fennemore, and McDaniel (1992) define the correlation length as the normalized first moment of the correlation function

$$l = \frac{\int_0^\infty \rho C_\zeta(\rho)d\rho}{\int_0^\infty C_\zeta(\rho)d\rho}. \tag{19}$$

Equation (19) is used in this paper for comparison with the YMcD model. The lag at which the correlation function crosses zero is used as the upper limit for the integrals in Eq. (19) because the most significant part of the correlation function is the region of small lags, and integrating to infinity can yield small or even negative correlation lengths, which does not make sense physically. The rms waveheight h and the correlation length l for Plant's D spectrum and the extended spectrum are given in Table II. The low-frequency extension is seen to have a small effect on h but a large effect on l, which is about five times larger.

To understand the effect of uncertainties in wind speed, fetch, and peak frequency, h and l are also calculated for two extreme cases. A "lowest-energy" spectrum is calculated using a wind speed of 6 m/s, a fetch of 1000 m, and a peak frequency of 0.27 Hz. Similarly a "highest-energy" spectrum is calculated using a wind speed of 10 m/s, a fetch of 4000 m, and a peak frequency of 0.19 Hz. As shown in Table II, using the highest and lowest energy spectra changes the rms waveheight by about a factor of 2 and the correlation length by about a factor of 1.5.

V. MODEL-DATA COMPARISON

In this section, the YMcD and XYMcD predictions are compared to measured SI for similar strength/rouhgness Φ and size/diffraction Λ parameters. For the measurements, Φ and Λ are calculated using the values of h and l shown in Table II, together with the source-receiver geometry. Model parameter values are given in Table III for the 13 SI measurements that are used in the paper. Data omitted because of

TABLE III. Parameters associated with the SI measurements presented here. See Fig. 6 for definition of paths. Also, θ is incident angle, f_c is center frequency, and Φ and Λ were defined in Eqs. (7) and (8). The model parameter values are calculated with h=4.4 cm and l=3.2 m (parameters of the swell enhanced Plant spectrum given in Table II).

Path	θ (deg)	f_c (kHz)	$\log_{10}(\Phi)$	Λ	Measurement number
P_1-H_4	12.6	20	0.16	1.1	1
		40	0.47	0.5	2
P_1-H_5	15.0	20	0.24	0.6	3
P_1-H_6	17.6	20	0.31	0.4	4
P_2-H_4	13.2	20	0.18	1.6	5
		40	0.49	0.8	6
P_2-H_5	15.6	20	0.26	1.0	7
		40	0.56	0.5	8
P_2-H_6	18.1	20	0.32	0.6	9
		40	0.62	0.3	10
P_3-H_4	13.7	20	0.20	1.9	11
P_3-H_5	16.1	20	0.27	1.2	12
P_3-H_6	18.7	20	0.33	0.8	13

projector and/or hydrophone directionality are P_1-H_5 at 40 kHz, P_1-H_6 at 40 kHz, P_3-H_4 at 40 kHz, P_3-H_5 at 40 kHz, and P_3-H_6 at 40 kHz. It can be seen in Table III that Λ ranges from 0.3 to 1.9 and $\log_{10}(\Phi)$ ranges from 0.16 to 0.62 for this set of measurements.

Measurements of SI from different measurement periods are "noisy." That is, large variations are observed from day to day, but no measurement period has a consistently higher or lower SI (regardless of source/receiver geometry or signal type). This is consistent with the environment remaining relatively constant throughout the experiment. In order to reduce noise in the SI measurements, results from the seven measurements are averaged.

A. Comparison of long pulse SI with YMcD model

Figure 10 shows SI measurements made using the long pulse and projector-hydrophone pairs for which the omnidirectional assumption is not seriously violated. The mean and mean ±1 standard deviation calculated over all seven measurement periods are shown. Data are grouped by size/diffraction parameter Λ equal to 1.9 (measurement numbers 5 and 11), 1.0 (measurement numbers 1, 6, 7, 12, and 13), 0.5 (measurement numbers 2, 3, 4, 8, and 9) and 0.3 (measurement number 10). Three YMcD model curves are plotted in Fig. 10. The solid curve corresponds to the extended spectrum with a wind speed of 8 m/s, a fetch of 2500 m, and a peak frequency of 0.23 Hz. These are the best estimates of the environmental conditions at the time of the experiment. The dashed curves give an idea of the variation in SI prediction due to environmental uncertainties. The upper curves are calculated using the "lowest-energy" spectrum (l=2.2 m), and the lower curves are calculated using the "highest-energy" spectrum (l=4.9 m). Parameters for these two spectra are shown in Table II. It can be seen in Fig. 10 that SI measured using the long pulse and omni directional projector-hydrophones generally follows the YMcD model predictions over the limited range of strength/roughness parameter Φ for which data are available.

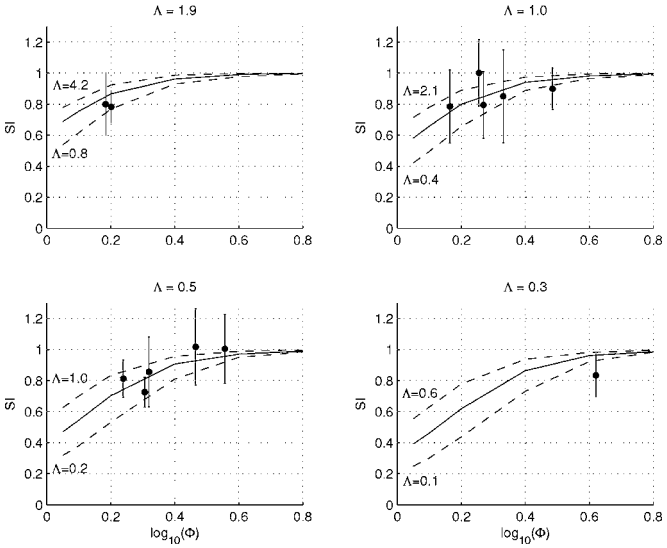

FIG. 10. Mean of SI measured over the seven measurement periods for the long pulse compared with model predictions for three environment conditions. Error bars denote the mean ±1 standard deviation. Parameters for the model predictions are given in Table II. The solid lines utilize the swell enhanced Plant spectrum with a wind speed of 8 m/s, a fetch of 2500 m, and a peak frequency of 0.23 Hz. The upper and lower dashed lines are calculated using the "lowest-energy" and "highest-energy" spectra, respectively.

B. Effect of signal bandwidth on SI

Dependence of SI on signal bandwidth (or temporal extent) is now discussed. Figure 11 shows mean measured SI for the long (1 ms) CW and 1 kHz LFM pulses, both of which possess a 1 kHz bandwidth, plotted using solid dots. Mean SI is shown for short (0.14 ms) CW and 7 kHz LFM pulses, both of which possess a 7 kHz bandwidth, plotted using open circles. CW and LFM data having the same effective bandwidth, or equivalently, temporal extent, are seen to have about the same SI values. Note that LFM signals are much longer (8 or 10 ms) than the CW signals, indicating that SI does not depend on the signal duration in a simple

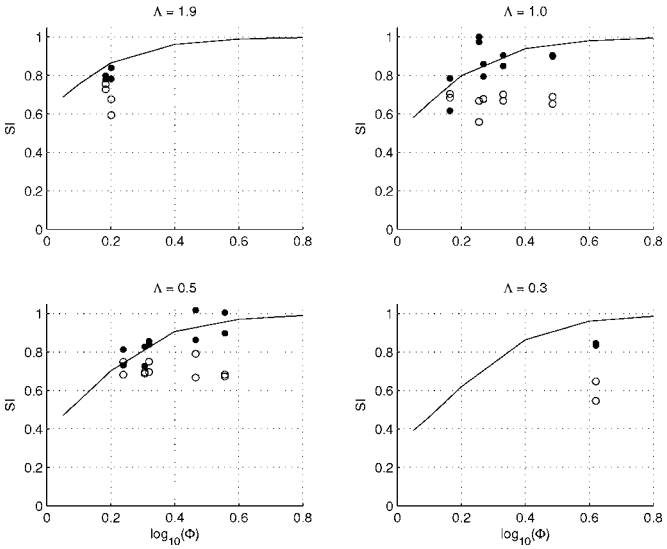

FIG. 11. Comparison of measured SI with the YMcD model for 1 kHz LFM and 1 ms CW signals (solid dots) and 7 kHz LFM and 0.14 ms CW signals (open circles).

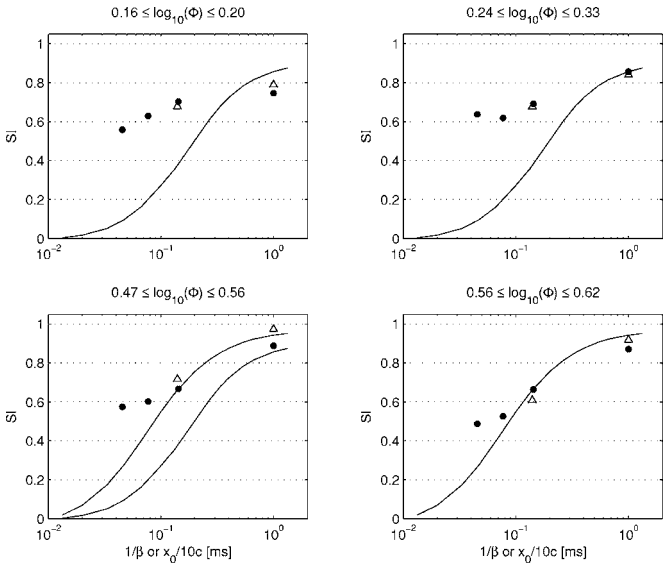

FIG. 12. Measured SI for LFM (solid dots) and CW data (open triangles) vs inverse signal bandwidth $1/\beta$ (equal to temporal extent after match filtering). SI measurements are grouped by values of Φ as indicated, and Λ is equal to 0.5 for all plots. For comparison, SI predicted using the XYMcD model is plotted vs $\frac{x_0}{10c}$ (solid lines), where x_0 is a measure of illumination factor width defined in Eq. (15). XYMcD predictions are calculated using $\log_{10}(\Phi)=0.4$ for the two first Φ groups, $\log_{10}(\Phi)=0.4$ and 0.6 for the third Φ group, and $\log_{10}(\Phi)=0.6$ for the last Φ group.

way. Figure 11 shows that measured SI is generally lower for signals with greater bandwidth (or smaller temporal extent), although for small values of $\log_{10}(\Phi)$ the trend is not as clear. Also the 1 kHz bandwidth (1 ms temporal extent) signals are in better agreement with the YMcD model predictions than the 7 kHz bandwidth (0.14 ms temporal extent) signals, which is consistent with the former being closer to the CW signal that is assumed by the YMcD model.

C. Comparison with the XYMcD model

Measured dependence of SI on signal bandwidth is now compared to the XYMcD model, which accounts for finite signal bandwidth and hydrophone beam width. Only the effect of signal bandwidth has been studied in the present paper. Figure 12 shows measured SI for both LFM and CW signals as a function of inverse signal bandwidth $\frac{1}{\beta}$, which (after match filtering) is equal to signal temporal extent. SI appears to increase approximately linearly with log inverse bandwidth. For comparison, Fig. 12 also shows SI computed using the XYMcD model and the illumination factor in Eq. (15) versus $\frac{x_0}{10c}$, where c is the speed of sound in water, and $\frac{1}{10}$ is chosen to fit SI measurements around the 1 ms temporal extent. The parameter x_0 is a measure of the width of the ensonified area, thus it is proportional to $\frac{c}{\beta}$. Strictly speaking the width of the ensonified area is given by $\frac{c}{\beta\cos\theta}$, but $\cos\theta$ is larger than 0.95 for all projector-receiver paths used in this paper so the angular dependence is neglected.

In Fig. 12, the SI measurements are partitioned into four groups according to Φ. XYMcD predictions are calculated for the value of $\log_{10}(\Phi)$ closest to the experimental values, except that computational difficulties limited model predictions to $\log_{10}(\Phi)\geq 0.4$. As mentioned in Sec. III, XYMcD model predictions depend very little on Λ for Λ between 0.3 and 1.9, and XYMcD predictions are given for $\Lambda=0.5$ only. The model predictions in the two upper panels of Fig. 12 are for $\log_{10}(\Phi)=0.4$, which is higher than that of the measurements. The model-data comparison is not particularly good, although the measured SI does increase with inverse bandwidth and the model prediction does increase with the ensonified area. The model predictions in the lower left panel of Fig. 12 are for $\log_{10}(\Phi)=0.4$ and $\log_{10}(\Phi)=0.6$. The $\log_{10}(\Phi)=0.6$ model prediction matches the data reasonably well for the lower bandwidth data. The model prediction in the lower right panel is for $\log_{10}(\Phi)=0.6$, and it also matches the lower bandwidth SI measurements reasonably well. In all panels the rates of decline do not agree very well, and there is some indication that some mechanism prevents measured SI from dropping below a threshold for the largest bandwidth. This point is discussed further in Sec. VI.

VI. DISCUSSION

The measurement-model comparison in Fig. 10 indicates that values of SI measured under conditions that did not seriously violate the continuous signal and omnidirection transducer assumptions of the YMcD model matched the trend of the model reasonably well. The range of Φ-Λ represented by the measurements is modest—certainly it would be valuable to measure SI under conditions that more fully explored the Φ-Λ parameter space. Figure 11 characterizes the clear dependence of measured SI on signal temporal resolution, or equivalently, inverse bandwidth. Higher bandwidth signals resulted in lower SI and poorer agreement with the YMcD model, which assumes continuous signals with infinitely narrow bandwidth.

Figure 12 shows that measured SI decreases from about 0.85 to about 0.5 as bandwidth increased from 1 to 22 kHz. A physical explanation is that smaller temporal extent resulting from increased bandwidth corresponds to a smaller ensonified surface area, so that fewer surface facets contribute to the received signal at any point in time; as a result fluctuations due to interference between micropaths are reduced. Figure 12 also contains SI predictions made using an extended (XYMcD) model, in which ensonified area is restricted via an illumination factor. The XYMcD model predicts a decrease in SI with reduced ensonified area consistent with the measured trend. However, the difference between the measurements and the XYMcD model predictions becomes large for the largest bandwidth measurements. The main reason for this discrepancy is thought to be the spatial averaging used in the model to calculate SI. As can be seen in Eq. (5) for the YMcD model, or in Eqs. (10) and (12) for the XYMcD model, SI is calculated by integrating contributions over the ocean surface, which corresponds to a spatial averaging. On the other hand the measured SI is calculated by temporal averaging (ping-to-ping averaging). When a large area of the ocean surface is ensonified, the two are equivalent. However, for small ocean surface ensonification, the number of contributions becomes small and the spatial averaging yields smaller SI than the temporal averaging does. To push this analysis to the extreme, when ocean sur-

face ensonification is very close to 0 (contributions from specular only), the mean intensity [see Eq. (10)] and the mean squared intensity [see Eqs. (12) and (13)] only depend on the normalized surface correlation function at zero lag which is 1; as a result the dependence on the surface statistics is removed and SI is equal to 0. That is why the XYMcD model predicts that SI tends to 0 when temporal extent tends to 0, as shown in Fig. 12. In the measurements, there is still ping-to-ping variations due to ocean "facets" moving with time, so SI does not decrease below a certain threshold that depends on the strength/roughness parameter Φ.

Two other bandwidth effects could be important. First the transmit voltage response (TVR) of the projectors used in the experiment is frequency dependent. This causes the effective bandwidth of the signals in the water to be lower for the 13 and 22 kHz bandwidth signals, and consequently moves the corresponding points in Fig. 12 to the right. Second, model predictions are performed at the center frequency (i.e., 20 or 40 kHz); for the largest bandwidth (and smallest temporal extent), many other frequencies are present in the received signal. This effect is not accounted for in the XYMcD model.

A caveat to the model-data comparison presented in this paper is that the YMcD model predicts SI due to interaction with the rough surface only, while the measured SI may be caused by other factors as well, such as inhomogeneities in the volume or near-surface bubbles. Thus generally speaking, for the measured SI

$$(\mathrm{SI})_{\mathrm{total}} = (\mathrm{SI})_{\mathrm{surf}} + (\mathrm{SI})_{\mathrm{other}} \geq (\mathrm{SI})_{\mathrm{surf}}, \tag{20}$$

where $(\mathrm{SI})_{\mathrm{total}}$ is the measurement result, $(\mathrm{SI})_{\mathrm{surf}}$ is that due to the interaction with the ocean surface, and $(\mathrm{SI})_{\mathrm{other}}$ is scintillation due to other effects. $(\mathrm{SI})_{\mathrm{surf}}$ is the quantity predicted by YMcD and XYMcD. Romond (2004) looked at the SI of the direct path for the same data set considered in the present study. The objective of that study was to investigate the effect of an intermittent current jet (localized in depth) on SI. Looking at four of the seven measurement periods only, Romond observed that SI was less than 0.1 for all projector-hydrophone pairs during three of the periods when the magnitude of the current jet was very low. However, during a measurement period when the current was higher, and for shallow projector-hydrophone pairs for which the direct path propagated through the current jet in a largely horizontal direction, the SI was found to be as high as 0.4 (the maximum value of 0.4 corresponded to P_3-H_1). Thus SI values greater than 0.1 were attributed to interaction of the acoustic waves with the current jet.

In the present study of SI for surface forward-reflected signals, shallow projectors and receivers could not be used. Surface-reflected rays connecting the deeper projector-hydrophone pairs propagate at much higher angles than the direct path rays and thus spend comparatively less time in the depth stratum where the current jet was observed. Therefore, since $(\mathrm{SI})_{\mathrm{total}}$ is always greater than 0.4 for surface forward-scattered signals, and surface bounce rays are steeper than direct path rays, $(\mathrm{SI})_{\mathrm{other}}$ should not significantly contribute to $(\mathrm{SI})_{\mathrm{total}}$ and $(\mathrm{SI})_{\mathrm{total}} \approx (\mathrm{SI})_{\mathrm{surf}}$.

VII. SUMMARY

Ocean measurements of scintillation index (SI) for acoustic signals forward scattered by the ocean surface have been presented and compared with a model by Yang and McDaniel (1991). To our knowledge, this is the first such comparison for ocean surface forward-scattered signals. The model uses the Kirchhoff approximation and assumes two-dimensional scattering geometry, CW signal, and omnidirectional projectors and hydrophones. The model utilizes two parameters: Φ which is proportional to surface roughness (strength or roughness parameter) and Λ which is a function of geometry and the surface waveheight correlation length (size or diffraction parameter). The experiment employed a range of geometries and signal frequencies, which in turn provided measurements over a range of values of Φ and Λ. The measurement took place close to, and on the leeward side of, San Clemente Island, with the result that the sea surface was quite benign and basically constant throughout the experiment. Measurements of SI reported here were averaged over the seven measurement periods. In general, measured SI was found to compare favorably with the Yang and McDaniel's model as long as the model assumptions (continuous signals and omnidirectional acoustic transducers) were not seriously violated. However, SI measured using signals with large bandwidth or directional transducers was lower than that predicted by the model. Approximately the same SI was measured using LFM signals and CW pulses having the same effective bandwidth, or equivalently, the same temporal extent, although the LFM signals were 8 to 70 times longer, indicating no simple dependence upon signal duration.

In order to investigate how increasing signal bandwidth (shorter temporal extent) reduces SI, the Yang and McDaniel model was extended to include an ocean surface illumination factor that controls the extent of the ocean surface that contributes to the scattered signal. SI predicted using the extended (XYMcD) model is found to decrease with decreasing ensonified surface area, but the relationship between ensonified area and signal temporal extent has not been quantified. Also, since spatial averaging is used in the model to calculate SI, XYMcD model predictions underestimate SI when the ensonified area is very small, which explains the discrepancy between model predictions and measured SI for the largest bandwidth signals. Although transducer directionality was not considered in the paper, it can be studied using the XYMcD model with an illumination factor corresponding to the projector/hydrophone directionality.

The YMcD and XYMcD models can be used to design future experiments. For instance, it is quite challenging to obtain SI measurements in the partially saturated region, where SI is above 1. However it can be done using short ranges and a range of acoustic frequencies, as long as the surface wave height elevation is not too small.

ACKNOWLEDGMENTS

Support by the Office of Naval Research is gratefully acknowledged. Special thanks go to Captain Jim Binford, USN (retired), NAVSEA PMS 415; Captain Bill Gaines,

USN (retired), and the technical staff of Marine Physical Lab, Scripps Institute of Oceanography; Penn State acoustics graduate students Tom Weber, Rachel Romond, and Steven Lutz; the Captains and crews of M/V Independence and M/V Acoustic Explorer. The authors also thank the reviewers for their constructive comments and suggestions.

[1]The Rayleigh roughness parameter is sometimes defined as $2\pi\frac{h\sin\theta}{\lambda}$ [see, for instance, Brown (1969) and Nichols and Senko (1974)].
[2]Personal communication with Al Todd of Axys Technologies.

Brown, M. V. (**1969**). "Intensity fluctuations in reflections from the ocean surface," J. Acoust. Soc. Am. **46**, 196–204.
Clay, C. S., and Medwin, H. (**1977**). *Acoustical Oceanography: Principles and Applications* (Wiley, New York).
Colosi, J. A., and Baggeroer, A. B. (**2004**). "On the kinematics of broadband multipath scintillation index and the approach to saturation," J. Acoust. Soc. Am. **116**, 3515–3522.
Dahl, P. H. (**1999**). "On bistatic sea surface scattering: Field measurements and modeling," J. Acoust. Soc. Am. **105**, 2155–2169.
Dahl, P. H. (**2004**). "Forward scattering from the sea surface and the van Cittert-Zernike theorem," J. Acoust. Soc. Am. **115**, 589–599.
Flatté, S. M. (**1983**). "Wave propagation through random media: Contributions from ocean acoustics," Proc. IEEE **71**(11), 1267–1294.
Flatté, S. M., Dashen, R., Munk, W. H., Watson, K. M., and Zachariasen, F. (**1979**). *Sound Transmission through a Fluctuating Ocean* (Cambridge University Press, Cambridge).
Frankenthal, S. (**1990**). "The bichromatic intensity correlation of radiation reflected off a randomly irregular surface," J. Acoust. Soc. Am. **87**, 2467–2476.
Macaskill, C., and Kachoyan, B. J. (**1988**). "Numerical evaluation of the statistics of acoustic scattering from a rough surface," J. Acoust. Soc. Am. **84**, 1826–1835.
McDaniel, S., and McCammon, D. (**1987**). "Composite-roughness theory applied to scattering from fetch-limited seas," J. Acoust. Soc. Am. **82**, 1712–1719.
Melton, D. R., and Horton, C. W. (**1970**). "Importance of Fresnel correction in scattering from a rough surface. I. Phase and amplitude fluctuations," J. Acoust. Soc. Am. **47**, 290–298.
Nichols, R. H., and Senko, A. (**1974**). "Amplitude fluctuations of low-frequency underwater acoustic pulses reflected from the ocean surface," J. Acoust. Soc. Am. **55**, 550–554.
Plant, W. J. (**2002**). "A stochastic, multiscale model of microwave backscatter from the ocean," J. Geophys. Res. **107**(C9), 3120–3140.
Romond, R. A. (**2004**). "The effect of near-surface ocean currents on high-frequency underwater acoustic signal intensity," Master's thesis, The Pennsylvania State University.
Scrimger, J. A. (**1961**). "Signal amplitude and phase fluctuations induced by surface waves in ducted sound propagation," J. Acoust. Soc. Am. **33**, 239–247.
Stroud, J. S., Marston, P. L., and Williams, K. L. (**1997**). "Intensity moments of underwater sound scattered by a Gaussian spectrum corrugated surface: Measurements and comparison with a catastrophe theory approximation," in *High Frequency Acoustics in Shallow Water*, edited by N. G. Pace, E. Pouliquen, O. Bergem, and A. P. Lyons (NATO SACLANT Undersea Research Centre, La Spezia, Italy), pp. 525–532.
Thorsos, E. I. (**1988**). "The validity of the Kirchhoff approximation for rough surface scattering using a Gaussian roughness spectrum," J. Acoust. Soc. Am. **83**, 78–92.
Thorsos, E. I. (**1990**). "Acoustic scattering from a "Pierson-Moskowitz" sea surface," J. Acoust. Soc. Am. **88**, 335–349.
Yang, C. C., Fennemore, G. C., and McDaniel, S. T. (**1992**). "Scintillation index of the acoustic field forward scattered by a rough surface for two- and three-dimensional scattering geometries," J. Acoust. Soc. Am. **91**, 1960–1966.
Yang, C. C., and McDaniel, S. T. (**1991**). "Fourth moments of acoustic waves forward scattered by a rough ocean surface," Waves Random Media **1**, 419–439.